Journal of Computational Science 26 (2018) 217–225

Contents lists available at ScienceDirect

Journal of Computational Science

journal homepage: www.elsevier.com/locate/jocs

Petascale simulations of compressible flows with interfaces☆

F. Wermelinger, U. Rasthofer, P.E. Hadjidoukas, P. Koumoutsakos*

Computational Science and Engineering Laboratory, ETH Zurich, Switzerland

ARTICLE INFO

Article history:
Received 31 October 2017
Accepted 28 January 2018
Available online 10 February 2018

Keywords:
High performance computing
Compressible multicomponent flow
Shock-capturing methods
Shock-induced bubble collapse
Cloud collapse

ABSTRACT

We demonstrate a high throughput software for the efficient simulation of compressible multicomponent flow on high performance computing platforms. The discrete problem is represented on structured three-dimensional grids with non-uniform resolution. Discontinuous flow features are captured using a diffuse interface method. A distinguishing characteristic of the method is the proper treatment of the interface zone as a mixing region of liquid and gas. The governing equations are discretized by a Godunov-type finite volume method with explicit time stepping using a low-storage Runge-Kutta scheme. The presented flow solver Cubism-MPCF is based on our Cubism library which enables a highly optimized framework for the efficient treatment of stencil based problems on multicore architectures. The framework is general and not limited to applications in fluid dynamics. We validate our solver by classical benchmark examples. Furthermore, we examine a highly-resolved shock-induced bubble collapse and a cloud of $\mathcal{O}(10^3)$ collapsing bubbles, which demonstrate the high potential of the proposed framework and solver.

1. Introduction

Cavitation refers to the rapid growth of vapor cavities in a liquid, followed by a violent collapse due to environmental pressure variations. It is known that cavitation causes material erosion on nearby surfaces, thus considerably reduces the expected lifespan of applications in marine propulsion, turbomachinery or fuel injection engines; see, e.g., [1]. Cavitating bubbles usually appear in a cloud which amplifies the destructive potential compared to the single bubble case. e.g., [2]. Nearby bubbles influence the dynamics of the collapse process compared to a single bubble confinement. Non-spherical collapses with focus towards the center of the cloud evolve, while the cloud collapses from the outer hull towards the center. Energy accumulates due to the earlier collapse of neighboring bubbles which is finally released in the form of a strong pressure wave emerging from the center of the cloud. Experimental results of collapsing bubble clouds were published, e.g., in [3–5]. Such setups pose a serious demand on measurement technologies. Numerical studies of cloud cavitation collapse try to alleviate these difficulties and provide additional insight to support the understanding of results observed in experimental studies; see [6,7].

Our aim is to perform detailed simulations of cavitating bubble clouds for the study of bubble-bubble and bubble-flow interactions. Therefore, we target at clouds with thousands of resolved cavities, that is, two orders of magnitude larger than the ones shown in [7]. Such simulations require not only an accurate model to treat the interface region correctly, but also highly efficient flow solvers to manage the large resolution requirement near interfaces. Diffuse interface methods for compressible multicomponent flow (see, e.g., [8–11]) resolve both fluid components by the computational grid. They do not treat the discontinuities at the interface, such as the jump in the density, in a sharp way, but introduce an artificial zone around the interface where the transition from one component to the other takes place in a smooth fashion. Therefore, these methods enable an adequate compromise between accuracy and computational efficiency. In the preceding study [12], we presented a compressible multicomponent flow solver, named Cubism-MPCF, with smoothed interface that is capable of processing grids with trillions of cells.

In this work, we investigate the performance of diffusive interface methods for compressible multicomponent flow and incorporate them into our open-source software Cubism-MPCF. We elaborate on the beneficial impact on the resolution requirements when properly treating the diffuse interface zone as a mixture of a liquid and a gas and not only as an artificial transition region from one component to the other. This is of paramount importance for achieving the targeted bubble counts. We further extend the work [13] by implementing non-uniform grids in our Cubism-MPCF soft-

☆ This is an extended version of our conference paper that was invited to the JoCS special issue (https://doi.org/10.1016/j.procs.2017.05.158).

* Corresponding author.
E-mail address: petros@ethz.ch (P. Koumoutsakos).

https://doi.org/10.1016/j.jocs.2018.01.008
1877-7503/

ware and widen the discussion about the behavior of the material interface in the discrete domain. To demonstrate the capabilities of the extended solver, we added simulation results of a highly-resolved 3D shock-induced collapse of a single bubble near a solid wall. Results for a cavitation tube test case are added to demonstrate the behavior of the material interface in a flow situation with strong pressure relaxation. Furthermore, we report on simulations of cloud cavitation collapse with $\mathcal{O}(10^3)$ cavities.

The paper is structured as follows: The governing equations and their discretization are introduced in Section 2. Section 3 provides an overview of our highly optimized flow solver Cubism-MPCF. Benchmark examples for validation as well as results from a highly-resolved shock-induced bubble collapse and a collapsing cloud of 2500 bubbles are presented in Section 4. We conclude our work in Section 5.

2. Computational method

2.1. Governing equations

The governing equation system, derived from the Baer-Nunziato model [14], reads as

$$\frac{\partial \alpha_1\rho_1}{\partial t} + \nabla\cdot(\alpha_1\rho_1\mathbf{u}) = 0, \tag{1}$$

$$\frac{\partial \alpha_2\rho_2}{\partial t} + \nabla\cdot(\alpha_2\rho_2\mathbf{u}) = 0, \tag{2}$$

$$\frac{\partial (\rho\mathbf{u})}{\partial t} + \nabla\cdot(\rho\mathbf{u}\otimes\mathbf{u} + p\mathbf{I}) = \mathbf{0}, \tag{3}$$

$$\frac{\partial E}{\partial t} + \nabla\cdot((E+p)\mathbf{u}) = 0, \tag{4}$$

$$\frac{\partial \alpha_2}{\partial t} + \mathbf{u}\cdot\nabla\alpha_2 = K\ \nabla\cdot\mathbf{u}, \tag{5}$$

where

$$K = \frac{\alpha_1\alpha_2(\rho_1 c_1^2 - \rho_2 c_2^2)}{\alpha_1\rho_2 c_2^2 + \alpha_2\rho_1 c_1^2}; \tag{6}$$

see e.g., [15,16] for derivation. This equation system comprises two mass conservation equations, one for each component, conservation equations for momentum and total energy in mixture-(or single-)fluid formulation as well as a transport equation for the volume fraction of one of the two components with source/sink term on the right-hand side, referred to as "K-div term" in the following. In Eqs. (1)–(5), $\mathbf{u}$ denotes the velocity, p the pressure, $\mathbf{I}$ the identity tensor, ρ the (mixture) density, E the (mixture) total energy $E = \rho e + 1/2\rho(\mathbf{u}\cdot\mathbf{u})$, where e is the (mixture) specific internal energy. Moreover, ρ_k, α_k and c_k with $k \in \{1, 2\}$ are density, volume fraction and speed of sound of the two components. It holds that $\alpha_1 + \alpha_2 = 1$ as well as $\rho = \alpha_1\rho_1 + \alpha_2\rho_2$ and $\rho e = \alpha_1\rho_1 e_1 + \alpha_2\rho_2 e_2$ for the mixture quantities.

The K-div term, originally derived in [17] for homogeneous mixtures, describes the reduction of the gas-volume fraction in a mixture of gas and liquid when a compression wave travels across the mixing region. For an expansion wave, it recovers the increase of the gas-volume fraction. The K-div term, which is only non-zero in the interface zone, is frequently neglected (see, e.g., [8,18,16]). However, treating the interface zone indeed as mixture of gas and liquid and not only as an artificial blending region from one component to the other is important for properly capturing the dynamics of collapsing bubbles, as already indicated by the results shown in [11]. Furthermore, this term also allows for dynamically creating interfaces, corresponding to the generation of gas pockets in low pressure regions; see, e.g., [10].

The equation system is closed by an appropriate equation of state for each of the pure fluids. To capture liquids and gases, the stiffened equation of state, which enables a simple, analytic approximation to arbitrary fluids, is applied; see, e.g., [19] for a review. It is given by

$$p = (\gamma_k - 1)\rho_k e_k - \gamma_k p_{c,k}, \tag{7}$$

where isobaric closure is assumed; see, e.g., [16]. Parameters γ_k and $p_{c,k}$ depend on the material. For $p_{c,k} = 0$ Pa and γ_k being the ratio of specific heats, the equation of state for ideal gases is recovered. Unless otherwise specified, $\gamma_1 = 6.59$ and $p_{c,1} = 4.069 \cdot 10^8$ Pa are used for water and $\gamma_2 = 1.4$ and $p_{c,2} = 0$ Pa for air.

2.2. Numerical method

System (1)–(5) is discretized using the method of lines. Our formulation builds on a finite volume method for uniform and non-uniform structured grids which are constant in time. Spatial operators are approximated using high-order stencil schemes. The approach yields a system of ordinary differential equations

$$\frac{d\mathbf{V}(t)}{dt} = \mathcal{L}(\mathbf{V}(t)), \tag{8}$$

where $\mathbf{V}$ is a vector of cell average values and $\mathcal{L}(\cdot)$ is a discrete operator that approximates the convective fluxes and the source term in the governing system. The temporal discretization of Eq. (8) is obtained by an explicit third-order low-storage Runge-Kutta scheme proposed in [20]. The computation of the numerical fluxes is based on a Godunov-type scheme using the approximate HLLC Riemann solver introduced for single-phase flow in [21]. The Riemann initial states are determined by a shock capturing fifth-order WENO reconstruction (see [22]). Following [23], the reconstruction is carried out using primitive variables, and the HLLC Riemann solver is adapted to Eq. (5) to prevent oscillations at the interface. As the non-uniform grid remains constant in time, the computation of the varying coefficients for the WENO reconstruction must be carried out once. Relations for the non-uniform WENO coefficients have been presented in [18]. The solution is advanced with a time-step size that satisfies the Courant-Friedrichs-Lewy condition. For the weighting coefficients of the Runge-Kutta stages, the values suggested in [24] are used, resulting in a total variation diminishing scheme.

3. Cubism-MPCF

The computational method presented in the previous section is implemented into Cubism-MPCF. Cubism-MPCF was presented in its original form in [12] and later further developed in [25,26]. The most important features of Cubism-MPCF are summarized in the following, additional details about design considerations can be found in the aforementioned references.

We define the computational kernels RHS, DT and UP for the processing of the full discretization. RHS stands for "right-hand side" and is responsible for the evaluation of the approximate Riemann problem. DT determines the admissible time-step size based on a global reduction. Finally, UP performs the Runge-Kutta update for a given set of weighting coefficients. The computational cost distribution of RHS, DT and UP is 90%, 2% and 8%, respectively (neglecting I/O operations).

The software is designed for high performance computing (HPC) and achieves a throughput of more than 700 Billion cells per second [12] with a peak performance of 14.4 Pflop/s on BlueGene/Q systems [25]. The code relies on our Cubism library which provides a framework for the efficient treatment of high-order stencil schemes (e.g., RHS) as well as straightforward point-wise operations, such as DT and UP. The Cubism framework is general and not limited to

applications in fluid dynamics. It can be used to implement any type of solver on structured Cartesian grids. The library supports uniform and stretched non-uniform grids. The latter is implemented based on a mapping method which supports user-defined functions that describe the non-uniform mesh spacing. The software is open-source and can be downloaded from our lab repository.[1,2]

3.1. Hierarchical data structure based on static size blocks

Cubism-MPCF makes use of a two-level hierarchical data structure utilizing cubic blocks of static size. Data within the blocks is stored in an array of structures (AoS) format. The computational domain is composed by a set of blocks arranged on a Cartesian topology, maintained by the Cubism library. The static size of the blocks is chosen such that cache utilization is maximized on multi-core architectures. The hierarchical structure allows for increased temporal locality of the data, which is a main concern for stencil operations. The vector $\mathbf{V}$ in Eq. (8) makes use of this hierarchical structure. The low-storage Runge-Kutta scheme further doubles the memory footprint for each block. The varying coefficients of the numerical scheme (for a non-uniform mesh) are computed per block and stored in additional 1D arrays for each spatial dimension. This additional memory footprint is about two orders of magnitude smaller compared to the main block data. The pre-computed coefficients significantly reduce the computational overhead of the numerical scheme compared to a more advanced adaptive multi-resolution strategy. Moreover, the overhead due to the additional memory accesses is negligible compared to the uniform case where coefficients can be hard-coded.

3.2. Parallelization and optimizations

The solver is parallelized with a hybrid paradigm using the MPI and OpenMP programming models. The software is split into three abstraction layers to separate specific optimizations, increase reusability of the code and allow for more efficient prototyping of new simulation cases. The realization of the domain decomposition and the inter-rank communication is accomplished on the cluster layer. The subdomains are of fixed size and organized on a Cartesian processor topology. The cluster layer is responsible for the dispatch of the grid blocks to the node layer. The performance optimization techniques used for the block processing on the cluster layer are described in [25]. The thread level parallelism (TLP) is exploited on the node layer using the OpenMP standard. We employ dynamic work scheduling and a parallel granularity of one block per thread to hide potential load imbalances during the processing of the dispatched blocks. Each thread exclusively works on one block at a time. The block data and ghosts, required for the evaluation of the stencil at block boundaries, are loaded into a per-thread work buffer. The intra-rank ghosts are obtained from loading fractions of the surrounding blocks, whereas inter-rank ghosts are obtained from a global buffer. The computational kernels are executed on the core layer, which are called from the executing thread on the node. The core layer exploits data level parallelism (DLP) and instruction level parallelism (ILP) by relying on explicit vectorization and code fusion techniques reported in [25,12]. In order to apply these techniques, the core layer transforms the AoS layout into a structure of arrays (SoA) by converting the data into slices arranged on a ring buffer. More details on software design regarding the parallelization strategy used in Cubism-MPCF can be found in [12].

[1] https://gitlab.ethz.ch/mavt-cse/Cubism.
[2] https://gitlab.ethz.ch/mavt-cse/Cubism-MPCF.

3.3. Strong and weak scaling

We evaluate the performance of our solver on the Piz Daint supercomputer at Swiss National Supercomputing Centre (CSCS). The machine consists of 5272 Cray XC30 compute nodes, each equipped with an Intel Xeon E5-2670 8-core SandyBridge CPU and an Nvidia Tesla K20X GPU. The executable code has been generated with the GNU C++ compiler (v4.8). Fig. 1 shows the detailed strong scaling on a single node with hyperthreading enabled. The size of the cubic blocks is set to 32 cells along each edge. Our code exhibits excellent strong scaling up to 8 cores. The additional gain due to hyperthreading is small because of the high per-thread cache utilization. The Craypat profiler reports a 95.3% hit ratio for the L1D cache and 99.5% for the L1D and L2D caches combined. Fig. 1 displays the weak efficiency across 4096 nodes. The work load on each node is composed of 4096 blocks, resulting in a memory footprint of 8 GB per node. The time to solution for this configuration is 18.3 s (one full time step). The code achieves excellent weak efficiency on the (almost) full machine. The loss in efficiency is due to the collective MPI all-reduce operation required to synchronize the admissible time-step size after the DT kernel finishes. The average time required by the block processing algorithm for each stage of the third-order Runge-Kutta scheme is 6.05 s and 6.13 s for 1 and 4096 nodes, respectively. The timings correspond to one evaluation of the RHS kernel on the whole domain. We achieve this almost perfect compute/transfer overlap by employing the methods explained in [25].

4. Numerical examples

4.1. One-dimensional problems

4.1.1. Liquid-gas shock tube

A 1D two-component shock tube, as considered, e.g., in [27], is examined first. The initial conditions in the domain $\Omega = [0, 1]$ m read as

$$(\rho, u, p, \alpha_2)_0 = \begin{cases} (1000.0\ \text{kg/m}^3, 0\ \text{m/s}, 1.0 \cdot 10^9\ \text{Pa}, 0) \\ \quad \text{for}\ \ 0\ \text{m} \leq x \leq 0.75\ \text{m}, \\ (10.0\ \text{kg/m}^3, 0\ \text{m/s}, 1.0 \cdot 10^5\ \text{Pa}, 1) \\ \quad \text{for}\ \ 0.75\ \text{m} < x \leq 1.0\ \text{m}. \end{cases}$$

The parameters of the stiffened-gas equation of state are set to $\gamma_1 = 4.4$ and $p_{c,1} = 6.0 \cdot 10^8$ Pa for the liquid in the left part and to $\gamma_2 = 1.4$ and $p_{c,2} = 0$ Pa for the gas in the right part. Results are evaluated at time $t = 0.234$ ms, comparing them to the curves obtained from an exact two-phase Riemann solver. Fig. 2 exemplarily depicts the solution for the density obtained without the K-div term, as it vanishes for this case due to $\nabla \cdot \mathbf{u} = 0$ at the interface. All results are in good agreement with the exact solution.

4.1.2. Cavitation tube

A cavitation tube, as, e.g., shown in [10,28], constitutes the second example considered in this section and illustrates the action of the K-div term. The initial conditions in the domain $\Omega = [0, 1]$ m are given by

$$(\rho, u, p, \alpha_2)_0 = \begin{cases} (1150.0\ \text{kg/m}^3, -100.0\ \text{m/s}, 1.0 \cdot 10^5\ \text{Pa}, 1.0 \cdot 10^{-2}) \\ \quad \text{for}\ \ 0\ \text{m} \leq x \leq 0.5\ \text{m}, \\ (1150.0\ \text{kg/m}^3, 100.0\ \text{m/s}, 1.0 \cdot 10^5\ \text{Pa}, 1.0 \cdot 10^{-2}) \\ \quad \text{for}\ \ 0.5\ \text{m} < x \leq 1.0\ \text{m}. \end{cases}$$

The setup represents two rarefaction waves in a liquid that contains a small amount of gas. The parameters of the stiffened-gas

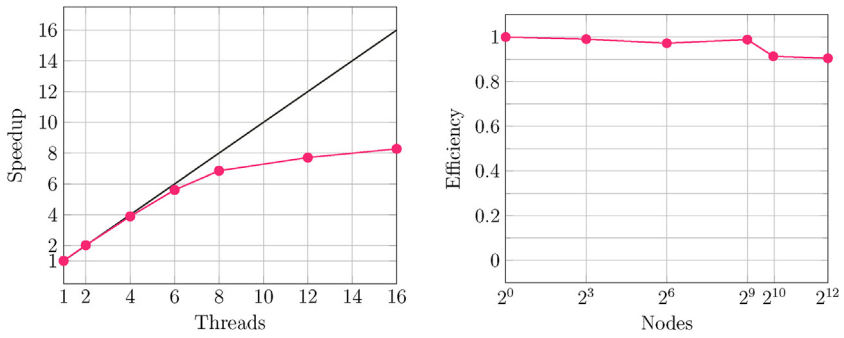

Fig. 1. Strong scaling on a single node (left). Weak scaling across 4096 nodes (right).

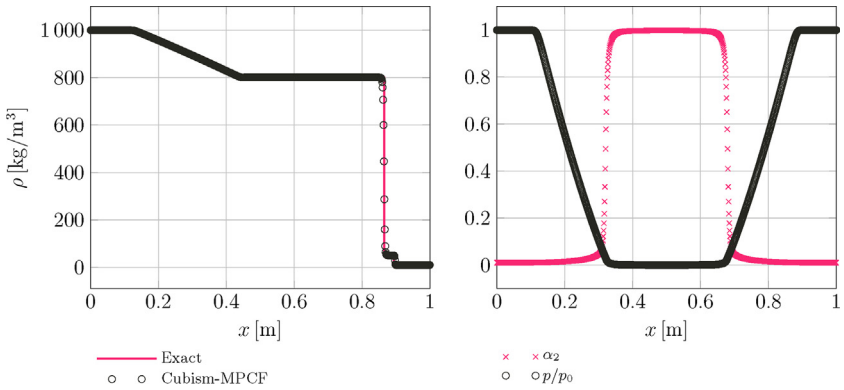

Fig. 2. Density of liquid-gas shock tube using 800 cells (left). Gas volume fraction and pressure of cavitation tube using 1000 cells (right).

equation of state are set to $\gamma_1 = 2.35$ and $p_{c,1} = 1.0 \cdot 10^9$ Pa for the liquid and to $\gamma_2 = 1.43$ and $p_{c,2} = 0$ Pa for the gas. Results are evaluated at time $t = 1.8$ ms. Fig. 2 displays the result for the gas-volume fraction and the pressure, which compare well to the ones shown in [10]. As the rarefaction waves move in opposite directions, the pressure in the center of the domain drops notably, but remains positive. The decrease of the pressure leads to the expansion of the gas such that a bubble of nearly pure gas is formed in the center. This gas expansion is enabled by the K-div term.

4.2. Single-bubble collapse

An isolated air bubble collapsing in water due to a prescribed jump between the initial pressure in the interior of the bubble, $p_{B,0}$, and the far-field, p_∞, is investigated next. A pressure ratio of $p_\infty/p_{B,0} = 10$ is considered. Initially, a zero-velocity field is assumed. The density of water amounts to $\rho_{1,0} = 1000\,\mathrm{kg/m^3}$ and of air to $\rho_{2,0} = 1\,\mathrm{kg/m^3}$. The initial radius $R_{B,0}$ of the bubble is set to 1 mm. The initial pressure and gas fraction field are given by

$$\alpha_{2,0} = \frac{1}{2}\left[1 - \tanh\left(\frac{r - R_{B,0}}{1.5h}\right)\right] \quad \text{and}$$

$$p_0 = \begin{cases} p_{B,0} & \text{if } \ 0 \le r \le R_{B,0}, \\ p_\infty + \dfrac{R_{B,0}}{r}(p_{B,0} - p_\infty) & \text{otherwise,} \end{cases}$$

where h denotes the cell length and r the distance between a point $\mathbf{x}$ of the domain and the center of the bubble; see [11]. The solution of the Keller-Miksis equation [29], which constitutes an ordinary differential equation for $R_B(t)$ in the weakly compressible case, serves as a reference for our investigations. The bubble radius from our 3D simulations is obtained based on the gas-volume fraction α_2 via

$$R_B = \sqrt[3]{3/(4\pi)\int \alpha_2 \mathrm{d}\Omega}\,.$$

Exploiting the symmetry of the problem, the computation domain is a cube of size $\Omega = [0, 15R_{B,0}]^3$, which contains one eighth of the bubble centered at the origin. Symmetry boundary conditions are imposed at the three faces of the cube intersected by the interface, while zeroth-order absorbing boundary conditions are assumed for the remaining faces. A grid refinement study is provided in Fig. 3. The initial bubble radius is resolved by approximately 12 cells for the coarser grid and by 25 cells for the finer one. When using the finer grid, differences between the 3D simulation and the solution of the Keller-Miksis equation are only marginal. Already with the coarser grid, the curve from the 3D simulation is close to the reference data. In addition, results obtained with a formulation neglecting the K-div term, which is also frequently used in literature for compressible multiphase flow (see, e.g., [18,16,12]), are included. A pronounced positive impact of the K-div term is observed for both resolutions. For the rather coarse resolutions used here, the minimum radius is reached at an earlier time and deviates significantly from the solution of the Keller-Miksis equation when the K-div term is omitted. Although convergence towards the reference curve can be stated, significantly higher resolutions would be required if the K-div term is omitted.

Furthermore, Fig. 3 illustrates the influence of the K-div term on the behavior of the interface thickness, which is defined as

$$d_I = R_{\theta=0.1} - R_{\theta=0.9} \tag{9}$$

based on two equivalent bubble radii. These radii are associated with the 0.1- and 0.9-iso-contours of the gas-volume-fraction field. The equivalent bubble radius is defined by $R_\theta = h\sqrt[3]{3/(4\pi)\sum_{l=1}^{n_c}\chi_\theta}$

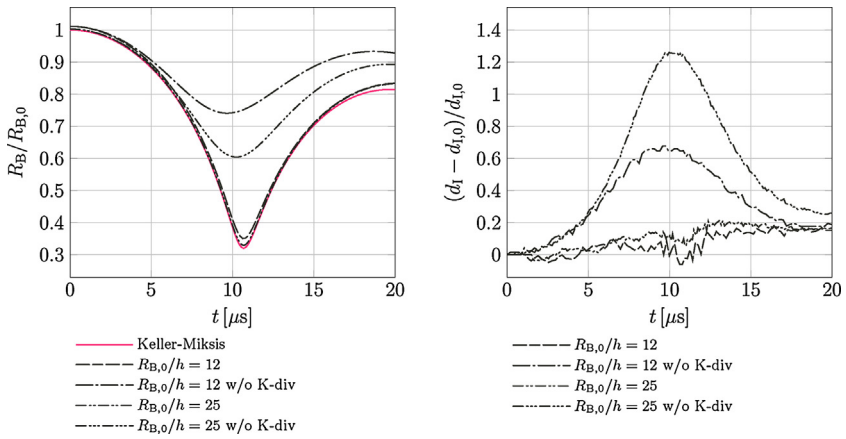

Fig. 3. Bubble radius R_B of single-bubble collapse at $p_\infty/p_{B,0} = 10$ (left). Evolution of interface thickness d_l of bubble (right).

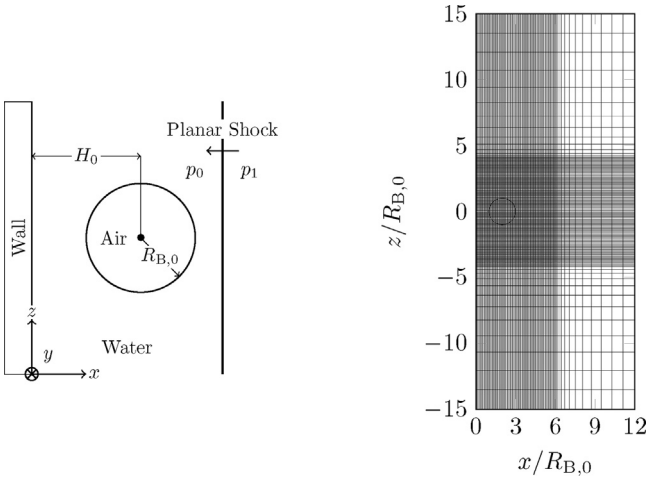

Fig. 4. Initial bubble configuration in a plane normal to the y-coordinate through the center of the bubble (left). Visualization of the computational mesh in the same plane, showing every twentieth grid point (right).

and uses a shifted phase indicator function χ_θ with threshold value θ, which is given by $\chi_\theta = 1$ if $\alpha_2 > \theta$ and $\chi_\theta = 0$ otherwise. In the definition of R_θ, h denotes the cell size and n_c the number of grid cells. The interface thickness increases approximately linearly in time when the K-div term is included. This increase can be almost exclusively attributed to numerical diffusion. Without the K-div term, the interface particularly thickens, reaching its maximum at the time of collapse. These investigations reveal the thickening of the interface when the K-div term is not considered, in turn leading to the time shift in the collapse process. Moreover, neglecting the K-div term appears to "stiffen" the system such that a further compression of the bubble is prevented, and large deviations from the expected minimum radius are observed; see Fig. 3. The stiffened behavior may be traced back to the simple advection of α_2. However, to ensure a correct thermodynamic behavior (see [30]), the gas content α_2 has to adapt to pressure changes in the mixture. Exactly this behavior is recovered by the K-div term. Therefore, the K-div term has to be considered for the present applications.

4.3. Shock-induced collapse of a single bubble near a solid wall

The shock-induced collapse of a single air bubble near a solid wall is presented next. The problem setup is sketched in Fig. 4. The bubble is initialized with radius $R_{B,0}$ and displaced by a stand-off distance $H_0 = 2R_{B,0}$ from the wall. The bubble is surrounded by liquid water, where both fluids are initially at rest with pressure p_0. A planar shock wave normal to the x-direction is initialized at coordinate $x = 3.15R_{B,0}$ with a strength of $p_1/p_0 = 353$. The liquid speed of sound ahead of the shock is $c_L = 1658$ m/s and the pressure is set to $p_0 = 1.0 \cdot 10^5$ Pa. The initial density of the liquid is set to $\rho_{1,0} = 998\,\mathrm{kg/m^3}$ and that of air to $\rho_{2,0} = 1\,\mathrm{kg/m^3}$. The material parameter for the stiffened equation of state are set to $\gamma_1 = 6.68$ and $p_{c,1} = 4.103 \cdot 10^8$ Pa for the liquid and to $\gamma_2 = 1.4$ and $p_{c,2} = 0$ Pa for the air. Both fluids are inviscid and time is expressed in non-dimensional form by $t^* = t/(R_{B,0}/c_L)$. A similar problem in a 2D domain is discussed in [31]. The extents of the computational domain are given by $[L_x \times L_y \times L_z] = [12 \times 15 \times 30]$, where all spatial dimensions are normalized with $R_{B,0}$. The domain is discretized using $1728 \times 1280 \times 2560$ cells with increased resolution in the neighborhood of the bubble, such that the initial bubble radius $R_{B,0}$ is resolved by 250 cells, see Fig. 4. Half of the bubble is simulated using a symmetry boundary condition. The wall is modeled with a reflecting boundary, where the impedance of the wall is assumed infinite. The remaining boundaries are absorbing.

Fig. 5 shows numerical schlieren images in the plane through the bubble center normal to the y-coordinate. The four different times illustrate the incident shock ($t^* = 1.614$), the impact of the upstream bubble wall on the downstream bubble wall ($t^* = 8.289$), the expansion of the generated water-hammer shock ($t^* = 8.449$) and the post-collapse phase ($t^* = 9.709$). The upstream bubble wall (proximal to the incident shock) starts to move towards the wall upon impact of the incident shock while the downstream bubble wall (distal to the incident shock) continues to remain at rest for a short instant after passing of the incident shock due to the shielding of the bubble. Fig. 6 shows the time history of the bubble wall velocities measured for the point proximal to the incident shock and the point distal to the incident shock. The proximal bubble wall experiences a high acceleration at the impact of the incident shock, followed by a low acceleration regime for about six time units. This slow regime is followed by a fast regime where the proximal wall velocity transitions to supersonic in roughly two time units and impacts on the distal bubble wall at $t^* = 8.289$, generating a strong water-hammer shock. The wall velocities are evaluated on the liquid side of the interface for a gas-volume fraction that corresponds to $\alpha_2 = 0.1$. A similar analysis has been presented in [31] where both velocities were reported in the subsonic regime. Our result captures a maximum bubble wall velocity that is in the supersonic regime, which is consistent with experimental results reported for spherical cavities [32].

Fig. 6 shows the time history for pressures, p_w, measured in four points along the y-axis on the solid wall. The shock reflection is observed after the time $t^* = 3$ where the wall pressure doubles in a point far away from the projected bubble center, while the

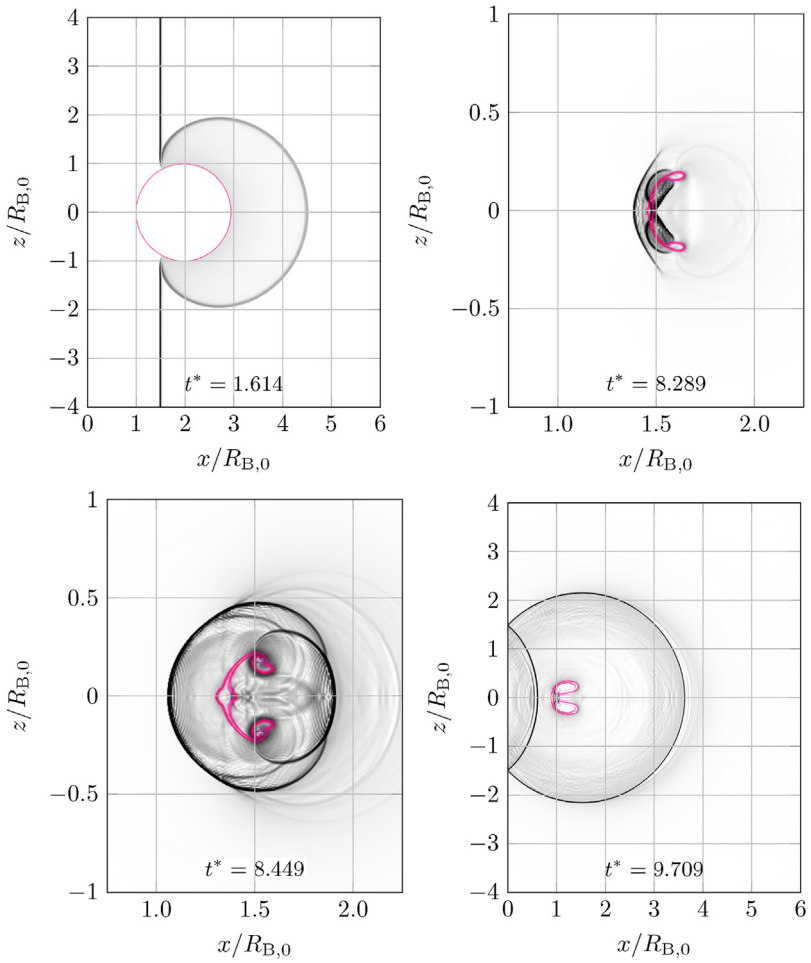

Fig. 5. Numerical schlieren images of the incident shock phase (top left) impact of upstream bubble wall on downstream bubble wall (top right), expansion of the water-hammer shock (bottom left) and post-collapse phase (bottom right). The images are computed in the plane through the initial bubble center. Rarefaction waves correspond to continuous gray regions and shock waves correspond to black narrow regions. The interface is shown in red color. (For interpretation of the references to color in this figure legend, the reader is referred to the web version of this article.)

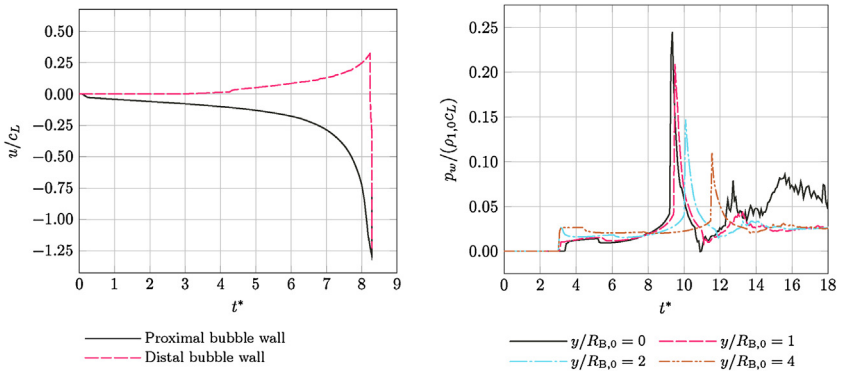

Fig. 6. Velocity measured in the point on the bubble wall that is closest to the incident shock, denoted by proximal bubble wall, and velocity of the point on the opposite side, denoted by distal bubble wall (left). Pressure measured on the solid wall in four points along the y-axis (right).

point corresponding to the projected bubble center $y/R_{B,0} = 0$ experiences a delay due to the diffraction of the incident shock upstream. The observed pressure drops are caused by rarefaction waves that are reflected back to the wall from the distal bubble interface. The maximum wall pressure $\max(p_w) = 0.67$ GPa is measured in the center point $y/R_{B,0} = 0$ at time $t^* = 9.342$. The time difference between the water-hammer initiation and the impact on the wall is slightly larger than one time unit since the distal bubble wall moves away from the solid wall during the collapse. The impact of the water-hammer shock on the solid wall causes material erosion and eventually reduces the lifespan of related applications. Moreover, a tensile pressure is measured in the point $y/R_{B,0} = 0$ shortly after the water-hammer impact, which generates secondary cavitation that leads to a further increase of the erosive potential on the wall surface.

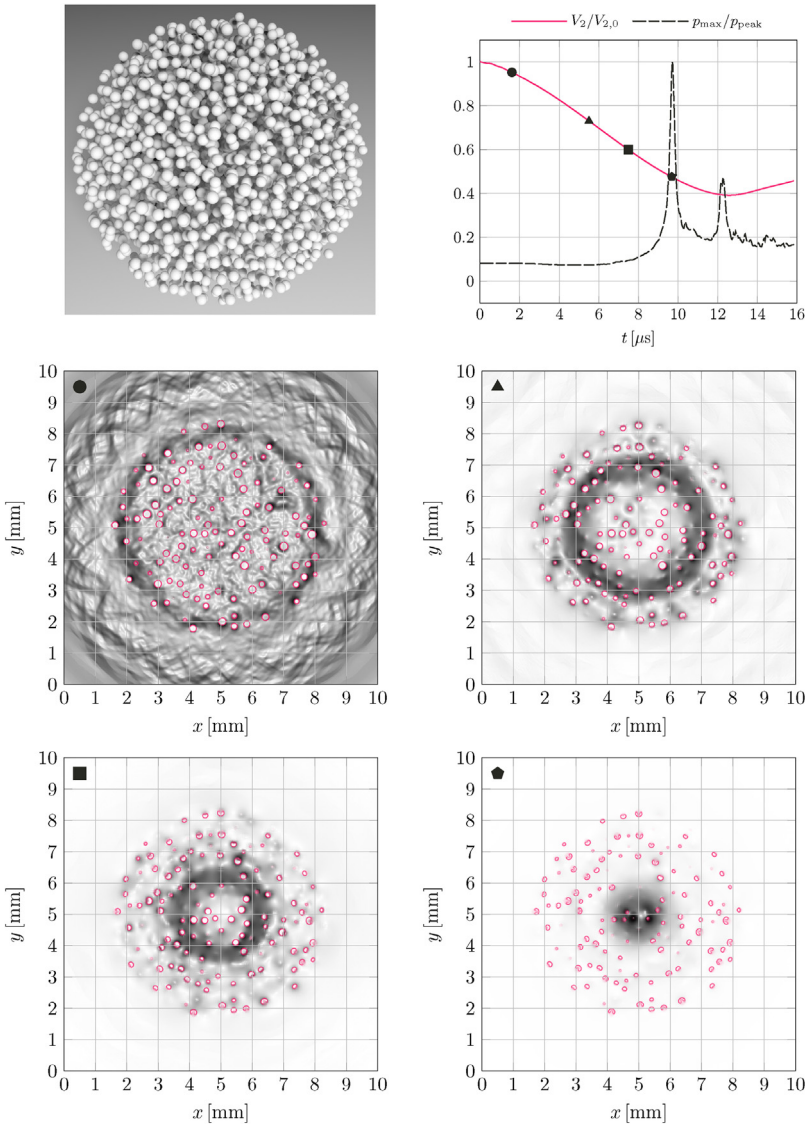

Fig. 7. Initial configuration of 2500 bubble cloud (top left). Normalized gas volume of cloud and maximum pressure versus time (bottom left). The remaining four figures illustrate (from left to right and from top to bottom) schlieren visualizations of the pressure gradient (monochrome color) and the bubble interfaces (red color) at the indicated time instants. (For interpretation of the references to color in this figure legend, the reader is referred to the web version of this article.)

4.4. Cloud cavitation collapse

In the following, results from a collapsing cloud comprising 2500 gas bubbles are presented. For the setup of the cloud, bubbles are randomly positioned within a sphere of radius $R_C = 3.5$ mm. The radius of the bubbles is also chosen at random from the interval [0.10;0.15] mm such that the average bubble radius amounts to 0.11 mm. While the positions of the bubbles are obtained from a uniform distribution, a log-normal distribution is used for their radii. The considered cloud contains a gas content of 8.4%, resulting in a cloud interaction parameter of $\beta = 85$ (see, e.g., [33] for a definition). The computational domain $\Omega = [0;10]^3$ mm^3 is discretized by 1024^3 cubic grid cells. Hence, the bubble radii are resolved by 10 to 15 cells. At the boundaries, non-reflecting, characteristic-based boundary conditions are applied; see, e.g., [34]. The bubble pressure is set to $p_{B,0} = 45$ bar. The ambient pressure is set to $p_\infty = 100$ bar, and the initial pressure field is determined as explained in [7]. Pressurized air with $\rho_{2,0} = 11.352$ kg/m^3 is assumed for the gas in the bubble and water with $\rho_{1,0} = 1000$ kg/m^3 for the surrounding liquid.

Fig. 7 displays the initial cloud, the evolution of the gas volume V_2 and the maximum pressure p_{max} as well as numerical schlieren images (see [35]) from the center plane of the cloud. Consistent with the experimental findings in [5], the peak of the maximum pressure appears several micro-seconds before the minimum volume is reached. The schlieren images show the formation of a spherical pressure wave, in accordance with the symmetry of the configuration. While the pressure wave propagates through the cloud, it increases in strength such that the highest pressures are observed in the core of the cloud. The pressure wave is accompanied by a subsequent strong deformation of the bubbles. The deformation of the bubbles is caused by inward-pointing micro-jets due to bubble–bubble interactions. As the imposed pressure ratio is rather low, the strength of the individual bubble collapses is relatively weak. Together with the relatively high β, we encounter a regime of weak collapse strength, but strong bubble interactions. As a result, most of the energy of the pressure jump is transferred into kinetic energy via the micro-jets. Owing to the strong micro-jets, all bubbles get pierced during the collapse process.

5. Conclusions

We have presented a compressible multicomponent flow solver for large scale simulation of cavitating flows. We have used a diffuse interface method to capture the interface on uniform and non-uniform structured grids. The computational approach is based on a Godunov-type finite volume method and has been implemented into our open-source software Cubism-MPCF. The software relies on the Cubism library which provides an HPC framework for the efficient treatment of high-order stencil schemes as well as point-wise operations. We have validated our approach for two classical benchmark examples, a liquid-gas shock tube and a single-bubble collapse. Using the latter test case, we have demonstrated the importance of recovering the compression and expansion of the gas in the interface zone when applying smoothed interfaces to compressible flow problems. Eventually, we have investigated a highly-resolved shock-induced bubble collapse and a cloud of 2500 collapsing bubbles, which have highlighted the high potential of the proposed approach and solver.

Ongoing and future research includes the investigation of collapsing clouds of $\mathcal{O}(10^4)$ gas bubbles, a comparative study with respect to approaches based on bubble-particle models, the inclusion of viscous and surface tension effects as well as developments towards software for heterogeneous compute architectures.

Acknowledgements

An award of computer time was provided by the Innovative and Novel Computational Impact on Theory and Experiment (INCITE) program under the project CloudPredict. This research used resources of the Argonne Leadership Computing Facility, which is a DOE Office of Science User Facility supported under Contract DE-AC02-06CH11357. We further gratefully acknowledge support by the European Research Council Advanced Investigator Award (FMCoBe 341117). This work also used computational resources granted by the Swiss National Supercomputing Centre (CSCS) under project ID s500 and s754.

References

[1] D.P. Schmidt, M.L. Corradini, The internal flow of diesel fuel injector nozzles: a review, Int. J. Engine Res. 2 (2001) 1–22.
[2] G. Chahine, Pressures generated by a bubble cloud collapse, Chem. Eng. Commun. 28 (1984) 355–367.
[3] N. Bremond, M. Arora, C.-D. Ohl, D. Lohse, Controlled multibubble surface cavitation, Phys. Rev. Lett. 96 (2006).
[4] E.A. Brujan, T. Ikeda, Y. Matsumoto, Shock wave emission from a cloud of bubbles, Soft Matter 8 (2012) 5777.
[5] K. Yamamoto, Investigation of bubble clouds in a cavitating jet, in: Mathematical Fluid Dynamics, Present and Future, Springer Nature, 2016, pp. 349–373.
[6] N.A. Adams, S.J. Schmidt, Shocks in cavitating flows, in: Bubble Dynamics and Shock Waves, Springer Nature, 2013, pp. 235–256.
[7] A. Tiwari, C. Pantano, J. Freund, Growth-and-collapse dynamics of small bubble clusters near a wall, J. Fluid Mech. 775 (2015) 1–23.
[8] G. Allaire, S. Clerc, S. Kokh, A five-equation model for the simulation of interfaces between compressible fluids, J. Comput. Phys. 181 (2002) 577–616.
[9] R. Saurel, R. Abgrall, A simple method for compressible multifluid flows, SIAM J. Sci. Comput. 21 (1999) 1115–1145.
[10] R. Saurel, F. Petitpas, R.A. Berry, Simple and efficient relaxation methods for interfaces separating compressible fluids, cavitating flows and shocks in multiphase mixtures, J. Comput. Phys. 228 (2009) 1678–1712.
[11] A. Tiwari, J.B. Freund, C. Pantano, A diffuse interface model with immiscibility preservation, J. Comput. Phys. 252 (2013) 290–309.
[12] D. Rossinelli, B. Hejazialhosseini, P. Hadjidoukas, C. Bekas, A. Curioni, A. Bertsch, S. Futral, S.J. Schmidt, N.A. Adams, P. Koumoutsakos, 11 PFLOP/s simulations of cloud cavitation collapse, in: Proceedings of the International Conference on High Performance Computing, Networking, Storage and Analysis, SC'13, ACM, New York, NY, USA, 2013, pp. 3:1–3:13.
[13] U. Rasthofer, F. Wermelinger, P. Hadjidoukas, P. Koumoutsakos, Large scale simulation of cloud cavitation collapse, Proc. Comput. Sci. 108 (2017) 1763–1772.
[14] M. Baer, J. Nunziato, A two-phase mixture theory for the deflagration-to-detonation transition (DDT) in reactive granular materials, Int. J. Multiph. Flow 12 (1986) 861–889.
[15] A. Murrone, H. Guillard, A five equation reduced model for compressible two phase flow problems, J. Comput. Phys. 202 (2005) 664–698.
[16] G. Perigaud, R. Saurel, A compressible flow model with capillary effects, J. Comput. Phys. 209 (2005) 139–178.
[17] A.K. Kapila, R. Menikoff, J.B. Bdzil, S.F. Son, D.S. Stewart, Two-phase modeling of deflagration-to-detonation transition in granular materials: reduced equations, Phys. Fluids 13 (2001) 3002–3024.
[18] V. Coralic, T. Colonius, Finite-volume WENO scheme for viscous compressible multicomponent flows, J. Comput. Phys. 274 (2014) 95–121.
[19] R. Menikoff, B.J. Plohr, The Riemann problem for fluid flow of real materials, Rev. Mod. Phys. 61 (1989) 75–130.
[20] J. Williamson, Low-storage Runge-Kutta schemes, J. Comput. Phys. 35 (1980) 48–56.
[21] E.F. Toro, M. Spruce, W. Speares, Restoration of the contact surface in the HLL-Riemann solver, Shock Waves 4 (1994) 25–34.
[22] G.-S. Jiang, C.-W. Shu, Efficient implementation of weighted ENO schemes, J. Comput. Phys. 126 (1996) 202–228.
[23] E. Johnsen, T. Colonius, Implementation of WENO schemes in compressible multicomponent flow problems, J. Comput. Phys. 219 (2006) 715–732.
[24] S. Gottlieb, C.-W. Shu, Total variation diminishing Runge-Kutta schemes, Math. Comput. Am. Math. Soc. 67 (1998) 73–85.
[25] P.E. Hadjidoukas, D. Rossinelli, B. Hejazialhosseini, P. Koumoutsakos, From 11 to 14.4 PFLOPs: performance optimization for finite volume flow solver, Proceedings of the 3rd International Conference on Exascale Applications and Software (2015).
[26] P.E. Hadjidoukas, D. Rossinelli, F. Wermelinger, J. Sukys, U. Rasthofer, C. Conti, B. Hejazialhosseini, P. Koumoutsakos, High throughput simulations of two-phase flows on Blue Gene/Q, in: Parallel Computing: on the Road to Exascale, Proceedings of the International Conference on Parallel Computing, ParCo 2015, 1–4 September 2015, Edinburgh, Scotland, UK, 2015, pp. 767–776.
[27] N. Favrie, S. Gavrilyuk, B. Nkonga, R. Saurel, Sharpening diffuse interfaces with compressible flow solvers, Open J. Fluid Dyn. 4 (2014) 44–68.
[28] R. Saurel, F. Petitpas, R. Abgrall, Modelling phase transition in metastable liquids: application to cavitating and flashing flows, J. Fluid Mech. 607 (2008) 313–350.
[29] J.B. Keller, M. Miksis, Bubble oscillations of large amplitude, J. Acoust. Soc. Am. 68 (1980) 628–633.
[30] R. Saurel, O. Le Métayer, J. Massoni, S. Gavrilyuk, Shock jump relations for multiphase mixtures with stiff mechanical relaxation, Shock Waves 16 (2007) 209–232.
[31] E. Johnsen, T. Colonius, Numerical simulations of non-spherical bubble collapse, J. Fluid Mech. 629 (2009) 231–262.
[32] R.H. Mellen, An experimental study of the collapse of a spherical cavity in water, J. Acoust. Soc. Am. 28 (3) (1956) 447–454.
[33] C. Brennen, G. Reisman, Y.-C. Wang, Shock waves in cloud cavitation, Twenty-First Symposium on Naval Hydrodynamics (1997).
[34] T.J. Poinsot, S.K. Lele, Boundary conditions for direct simulations of compressible viscous flows, J. Comput. Phys. 101 (1992) 104–129.
[35] J.J. Quirk, S. Karni, On the dynamics of a shock-bubble interaction, J. Fluid Mech. 318 (1996) 129–163.

Fabian Wermelinger is a PhD student in the Computational Science and Engineering Laboratory at ETH Zurich. He received his MSc. in mechanical engineering from ETH Zurich in 2015. His research interests include modeling of multicomponent flows, cavitation phenomena and turbulence. Given the computational complexity of these problems, he is further concerned with software development for high performance computing and data compression algorithms.

Ursula Rasthofer obtained her diploma in aeronautics and aerospace from Technische Universität München (TUM) in 2009, and her PhD in mechanical engineering from TUM in 2015. She has been a postdoctoral researcher at ETH Zurich from 2015–2017. Her research interest focuses on modeling and simulation of turbulent flow, numerical methods for multiphase flow and high performance computing.

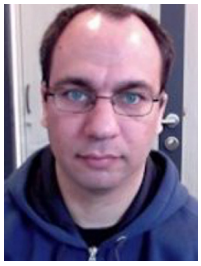

Panagiotis Hadjidoukas received his PhD in 2003 from the Computer Engineering and Informatics Department, University of Patras, Greece. Currently, he is a senior researcher and lecturer at ETH Zurich. His research interests include high performance computing on modern architectures and parallel frameworks for numerical optimization and uncertainty quantification. He is recipient of the ACM Gordon Bell Prize for peak performance in 2013.

Petros Koumoutsakos is Professor of Computational Science at ETH Zurich (2000–present). He received his PhD in Aeronautics and Applied Mathematics from the California Institute of Technology (1992). He conducted postdoctoral studies at the Center for Parallel Computing (Caltech, 1992–1994) and at the Center for Turbulence Research (Stanford U./NASA Ames, 1994–1997). Petros has been elected Fellow of the American Society of Mechanical Engineers (ASME), the American Physical Society (APS) and the Society of Industrial and Applied Mathematics (SIAM). He is recipient of the Advanced Investigator Award by the European Research Council and led the team that won the ACM Gordon Bell prize in Supercomputing (2013). In 2016 he was elected Fellow of the Collegium Helveticum.